Integrated Non-sliced OAWM Engine Enabling 320 GHz Photonic-Electronic Analog-to-Digital Conversion

D. Drayss[1,5], D. Fang[1,5], A. Quint[2], L. Valenziano[2], M. Lauermann[3], G. Lihachev[4], Y. Chen[1], H. Peng[1], S. Randel[1], T. Zwick[2], W. Freude[1], T. J. Kippenberg[4], and C. Koos[1]

(1) Inst. of Photonics and Quant. Elect. (IPQ) and Inst. of Microstruct. Techn. (IMT), Karlsruhe Inst. of Technology (KIT), Germany
(2) Institute of Radio Frequency Engineering and Electronics (IHE), Karlsruhe Institute of Technology (KIT), Germany
(3) Vanguard Automation GmbH, Gablonzer Straße 10, 76185 Karlsruhe, Germany
(4) Institute of Physics, Swiss Federal Institute of Technology Lausanne (EPFL), CH-1015 Lausanne, Switzerland
(5) Contributed equally daniel.drayss@kit.edu, christian.koos@kit.edu

Abstract: We demonstrate an optically and electrically packaged silicon photonic receiver system for non-sliced optical arbitrary waveform measurement (OAWM). The OAWM engine is used for high-speed data transmission and for photonic-electronic analog-to-digital conversion at bandwidths of up to 320 GHz. © 2024 The Author(s)

1. Introduction

Optical arbitrary waveform measurement (OAWM) based on frequency combs gives access to the full-field information of broadband optical signals [1]. Applications range from optical communications [2,3] to ultra-broadband photonic-electronic analog-to-digital conversion [4,5] and radar technology [6]. Among a variety of different OAWM schemes explored over the previous years [1-5], so-called non-sliced OAWM [3] is particularly interesting since it does not require high-quality slicing filters to decompose the broadband optical input signal into narrowband tributaries. However, while non-sliced OAWM is perfectly suited for efficient implementation using high-density photonic integrated circuits (PIC), all demonstrations of this scheme have so far relied on either discrete fiber-optic components [3] or on bare photonic dies that were optically and electrically probed during the experiments [7]. These laboratory implementations are clearly unsuited to serve as building blocks of more complex systems and to deliver on the promising potential of OAWM in its various applications.

In this paper, we present the first optically and electrically packaged OAWM engine. The device comprises a silicon photonic non-sliced OAWM receiver and relies on a Kerr frequency comb as a multi-wavelength local oscillator [8]. The optical acquisition bandwidth amounts to 320 GHz – the highest value so far demonstrated for an OAWM receiver having co-integrated photodiodes. We demonstrate the viability of the OAWM engine both in a high-speed data transmission experiment and as a subsystem of a 320 GHz photonic-electronic analog-to-digital converter (PE-ADC). To the best of our knowledge, our experiments represent the first demonstration of a PE-ADC system based on an integrated OAWM module. We believe that our work opens a path towards out-of-lab use of compact OAWM engines and ultra-broadband PE-ADC.

2. Non-sliced silicon photonic OAWM engine

The concept and implementation of the non-sliced OAWM engine is illustrated in Fig. 1(a) and Fig. 1(b). The receiver PIC (Rx PIC) comprises an array of IQ receivers (IQR), which are fed by the full optical input signal as well as by time-delayed copies of the local oscillator (LO) comb, Fig. 1(a). The electrical output signals of the various IQ receivers hence contain superimposed mixing products of all LO tones with the respective adjacent portions of the signal spectrum, which allows for reconstructing the full optical input signal using digital signal processing (DSP), see [3] for details. Our implementation relies on a compact (1.55 × 1.05 mm²) silicon PIC that comprises power splitters, delay lines, and four single-polarization IQR and that is optically connected to optical fibers via photonic wire bonds (PWB) [9,10], and electrically connected to an alumina fan-out printed circuit board (PCB) via metal wire bonds, see Fig. 1(b). The fan-out PCB contains biasing circuits and coaxial connectors to extract the overall eight RF signals. Coaxial cables connect the fan-out PCB to two synchronized Keysight UXR series oscilloscopes, which serve as an ADC array. We calibrate the OAWM receiver using an optical reference waveform of known shape, generated by a solid-state mode-locked femtosecond laser (Menhir 1550), see [3] for details. After calibration, the OAWM system can be fully described by an overall 32 complex-valued frequency responses that are associated with the

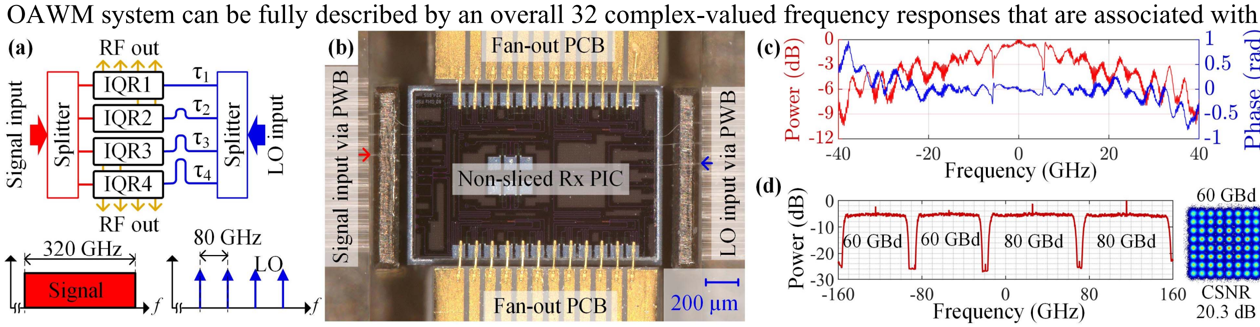

Fig. 1. Concept and implementation of the integrated non-sliced OAWM engine. **(a)** Conceptual setup of non-sliced OAWM with four IQ receivers (IQR). The optical input signal (320 GHz bandwidth) is split into $N=4$ copies and routed to an IQR array. The optical frequency comb (free spectral range $f_{\mathrm{FSR}}=80\,\mathrm{GHz}$) is split into four identical copies, which are delayed by $\tau_\nu \approx (\nu-1)/(N f_{\mathrm{FSR}})$, $\nu=1,\ldots 4$, on their way to the IQR array, where they serve as multi-wavelength local oscillators (LO). The generated RF output signals are acquired by a synchronized ADC array (Keysight UXR series oscilloscopes, not shown). **(b)** Microscope image of the electrically and optically packaged receiver photonic integrated circuit (Rx PIC) comprising power splitters, delay lines, and 4 IQR. The Rx PIC is connected via photonic wire bonds (PWB) to optical fibers and via metal wire bonds to a printed circuit board (PCB). All PWB were printed using the Sonata 1000 from Vanguard automation (Resist: Vancore B). **(c)** Exemplary measured frequency response comprising the optical (waveguides, splitters, photodiodes) and electrical (RF PCB, connectors, coaxial cables) characteristics of the OAWM engine. **(d)** Spectrum of an acquired 320 GHz-wide optical waveform, comprising four data channels (left) along with exemplary constellation diagram and estimated constellation signal-to-noise ratios (CSNR) (right).

in-phase and quadrature components of the four IQ receivers and the four LO comb tones [11]. These frequency responses comprise the optical characteristics of the on-chip waveguides, splitters, and photodiodes, as well as the electrical characteristics of the RF PCB and the attached coaxial cables, including also potential crosstalk, see Fig. 1(c) for a measured example. Note that the spectral ripples in the frequency response result from an impedance mismatch between the high-impedance photodetectors and the 50 Ω transmission lines and spurious reflections at the coaxial connectors, which might be mitigated by an optimized RF designs in the future.

3. Demonstration as optical receiver

In a first experiment, we demonstrate the performance of our non-sliced OAWM engine by using it as an optical receiver. In this experiment, the LO comb is generated by a fiber-packaged soliton microcomb, and the acquired optical signal consists of four wavelength-division multiplexed (WDM) 64QAM signals with symbol rates of up to 80 GBd covering a bandwidth of 320 GHz, Fig. 1(d). To the best of our knowledge, this represents the highest acquisition bandwidth so far achieved by an integrated OAWM engine. In our experiment, we find bit-error ratios (BER) between 1.6×10^{-3} and 7×10^{-3} for the four channels, which is well below the limit of soft-decision forward-error correction (FEC) with 20% overhead [4]. While this demonstrates the viability of the scheme, the performance can be further improved, e.g., by using a comb with a higher optical output power and hence an optical carrier-to-noise ratio (OCNR) that exceeds the current values between 19 dB and 22 dB.

4. Photonic-electronic ADC demonstration

In a second experiment, we use the OAWM engine as a building block of a more complex PE-ADC system. To this end, we combine the module with a broadband thin-film lithium-niobate (TFLN) Mach-Zehnder modulator (MZM, Hyperlight Corp.) to capture RF signals from DC to 320 GHz. The experimental setup is shown in Fig. 2(a). To overcome the OCNR limitations of the Kerr comb used in the OAWM experiment, the frequency comb is now generated by modulating the output of a continuous wave fiber-laser (NKT Photonics Koheras Adjustik), leading to comb tones at discrete frequencies $f_\nu = f_0 + \nu f_{\mathrm{FSR}}$, where f_0 =192.669 THz (λ_0 =1556 nm) is the frequency of the tone used as an optical carrier for the RF signal of interest, and where f_{FSR} = 39.97 GHz is the line spacing of the comb, see Inset Ⓐ of Fig. 2(a) for an illustration of the comb spectrum. The comb is amplified by an erbium-doped fiber amplifier (EDFA1) and spectrally split by a wavelength-selective switch (WSS) into an upper signal path comprising the optical carrier at frequency f_0 (red in Inset Ⓐ) and into a lower LO path comprising four comb lines at frequencies f_1, f_3, f_5, f_7 (blue in Inset Ⓐ). The optical carrier is amplified by EDFA2, filtered by a bandpass filter (BP), and fed to the high-speed TFLN-MZM, which is biased at the null point and driven by the RF signal under test. As the TLFN-MZM is subject to a roll-off of ~15 dB at 320 GHz, see red line in Fig. 2 (b), we additionally use a programmable optical filter (Finisar Waveshaper) as an optical equalizer to partially compensate the frequency response of the TFLN MZM in the optical domain – the associated optical transmission spectrum is indicated as a blue trace in Fig. 2(b). After the optical equalizer, the signal is amplified by EDFA5, bandpass-filtered to suppress amplified spontaneous emission (ASE) noise, and fed to the non-sliced OAWM engine. Proper reconstruction of arbitrary signals by non-sliced OAWM may require additional pilot tones [11], which are added at the input of the OAWM engine. Despite the optical equalization, the combined EO frequency response of the MZM and the optical equalizer is not fully flat and exhibits a dip around 300 GHz, see measured blue trace in Fig. 2(c). This dip is attributed to periodic structures on the TFLN die and may be avoided by an optimized MZM design in the future. We account for the residual MZM response and the dip at 300 GHz by digital post-equalization, which results in an overall flat system response, green trace in Fig. 2 (c), but leads to noise enhancement, especially around the dip at 300 GHz. For an absolute calibration of the PE-ADC system, the overall conversion factor associated with the spectrally flat response is finally measured using an RF input signal with a known voltage swing. Note that the phase response of the MZM is currently not corrected for, which may result in additional distortions around the dip at 300 GHz.

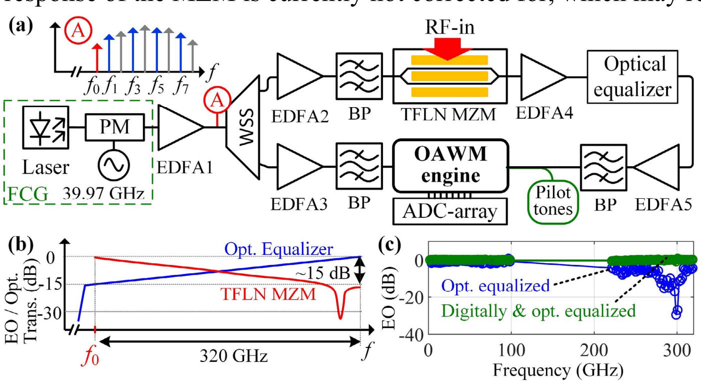

Fig. 2. Demonstration of photonic-electronic analog-to-digital conversion, combining the non-sliced OAWM engine with a high-speed thin-film lithium niobate (TFLN) Mach-Zehnder modulator (MZM). **(a)** Experimental setup: Frequency-comb generator (FCG), phase modulator (PM), erbium-doped fiber amplifier (EDFA), wavelength-selective switch (WSS), optical bandpass filter (BP). Inset Ⓐ: Illustration of comb spectrum with carrier (red, frequency f_0) and LO tones (blue, frequencies f_1, f_3, f_5, f_7). **(b)** Sketch of electro-optic (EO) frequency response of the TFLN MZM (red) and of the transmission spectrum of the optical equalizer (blue). **(c)** Measured EO frequency response of optically equalized TFLN MZM (blue) and additionally digitally equalized system frequency response (green).

The results of the PE-ADC experiments are summarized in Fig. 3. We first measure sinusoidal test tones in the bands 2-67 GHz, 70-110 GHz, and 220-320 GHz, generated either directly by an RF synthesizer (Keysight PSG E8257D) or via RF multipliers (Keysight SGX WR 10, and WR3.4). Two exemplary waveforms at 11 GHz and 320.2 GHz are shown in Fig. 3(a). From these measurements, we estimate the effective number of bits (ENOB) of the PE-ADC. Generally, the ENOB is obtained from the signal-to-noise-and-distortion ratio (SINAD) for a full-scale sinusoidal test tone that is fed to the system. For PE-ADC, the full-scale input range (FSIR) is eventually dictated by the nonlinearities of the cos-shaped MZM amplitude transfer function. To analyze this effect, we sweep the RF power of an 11 GHz sinusoidal test tone, extract the various noise and distortion contributions, quantified by the ratio of the associated power to the power of the test tone, and calculate the resulting SINAD as the inverse of the sum of all these contributions, see Fig. 3(b). For low RF powers, the ASE noise of the various EDFA represents the dominant

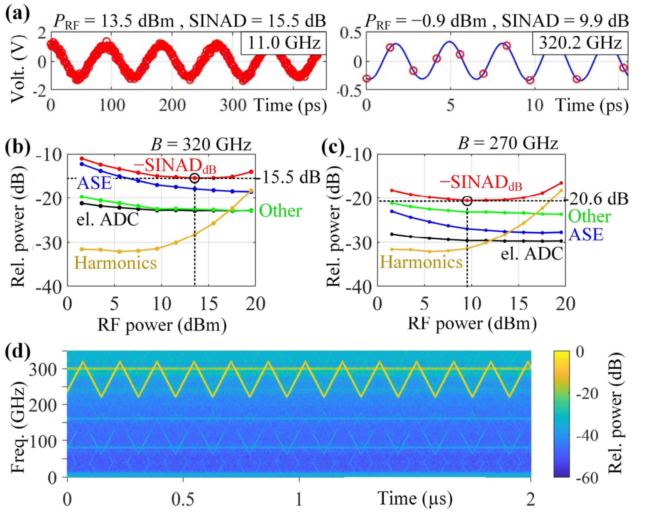

Fig. 3. Experimental PE-ADC demonstration. **(a)** Measured RF test tones at 11 GHz and 320.2 GHz **(b, c)** Relative power of noise and distortions with respect to the 11 GHz test tone at different RF input power levels. Amplified spontaneous emission (ASE, blue), electric ADC noise (gray), harmonics (yellow) and other distortions (green) are separated. The inverse signal-to-noise-and-distortion ratio (-SINAD$_{dB}$, solid red line) is obtained by adding all noise and distortion contributions. Subfigure (b) refers to the device used in our experiment, whereas Subfigure (c) indicates the estimated performance of an equivalent 270 GHz PE-ADC that is operated with a better frequency comb source. The black circles indicate the maximum achievable SINAD of 15.5 dB and 20.6 dB, from which the respective ENOB values of 2.3 and 3.1 are derived. **(d)** Spectrogram of a measured FMCW signal having a bandwidth of ~100 GHz and a center frequency of 270 GHz.

limitation, whereas the noise of the electronic ADC ('el. ADC noise'), the second- and third-order harmonics resulting, e.g., from MZM nonlinearities ('Harmonics'), and the remaining distortions ('Other') are significantly weaker. The remaining distortions comprise the optical pilot tones, signal-signal beat interference (SSBI) due to imperfect receiver balancing as well as spectral 'IQ images' caused by imperfect calibration of the IQ receivers. For increasing RF powers, the relative power of the third-order harmonics caused by the MZM increases and eventually evolves into a dominant limitation of the SINAD. A maximum SINAD of 15.5 dB, corresponding to an ENOB of 2.3, is reached at an RF input power of 13.5 dBm, corresponding to a full-scale peak-to-peak voltage swing of 3.0 V, see black circle in Fig. 3(b). It should be noted that the trace 'Harmonics' in Fig. 3(b) also comprises harmonic distortions of the synthesizer used for generating the test tone. This leads to a constant relative contribution at low RF powers instead of the theoretically expected slope between 1 and 2 in the log-log plot. The relatively low ENOB of 2.3 is mainly caused by two effects: First, the digital equalization of the dip in the MZM frequency response, Fig. 2(c), boosts both the ASE noise and the ADC noise. Second, the carrier at frequency f_0 was weak and featured a rather low OCNR of approximately 23 dB (reference bandwidth 12.5 GHz) upon amplification, which additionally distorts the signal. If the bandwidth of the PE-ADC is reduced from 320 GHz to 270 GHz to avoid the transmission dip, then the ENOB increases to 2.9 bit. Using additionally a comb source with better OCNR would further boost the SINAD to 20.6 dB and the ENOB to 3.1 – this scenario is indicated in Fig. 3(c). Note that we deliberately chose a relatively low frequency of 11 GHz for the test tone in the ENOB measurement for several reasons: First, nonlinear distortions, which limit the FSIR, will become weaker at higher frequencies, as the EO frequency response of the MZM decreases, Fig. 2(b). Test tones at high frequencies would hence lead to an overestimate of the FSIR and hence of the ENOB. Moreover, the ENOB characterization requires a high-quality signal source that can drive the MZM over its full range, which is straightforward at low frequencies, but challenging at high frequencies. Since the frequency response of our system has been digitally equalized and since the measurement of the 11 GHz test tone already comprises distortions across the entire acquisition bandwidth, we expect that the estimated SINAD of 15.5 dB and 20.6 dB, respectively, can be maintained also for higher test-tone frequencies. In a last experiment, we use an arbitrary waveform generator (Keysight M8199B) at the input of the 9× RF multiplier to generate an approximately 100 GHz-wide frequency-modulated continuous-wave (FMCW) signal centered at 270 GHz, which we directly measure using the PE-ADC, see Fig. 3(c) for the spectrogram. Such FMCW signals are typically used in radar applications. The signal shown in Fig. 3(c) corresponds to a theoretical resolution limit of 1.5 mm.

5. Summary

We have demonstrated the first optically and electrically packaged OAWM engine. Our implementation is based on the concept of non-sliced OAWM and relies on a silicon photonic integrated circuit (PIC) to capture optical waveforms with bandwidths up to 320 GHz. We show the viability of the OAWM engine for reception of high-speed optical communication signals and as a building block of a photonic-electronic analog-to-digital converter. We believe that our work opens a path towards out-of-lab use of compact OAWM engines and towards using ultra-broadband PE-ADC in practical applications.

This work was supported by the ERC Consolidator Grant TeraSHAPE (# 773248), by the EU H2020 project TeraSlice (# 863322), by the DFG projects PACE (# 403188360) and GOSPEL (# 403187440), by the joint DFG-ANR projects HybridCombs (# 491234846) and QuadCombs (# 505515860), by the DFG Collaborative Research Centers (CRC) WavePhenomena (SFB 1173, # 258734477) and HyPERION (SFB 1527, # 454252029), by the DFG Excellence Cluster '3D Matter Made to Order' (EXC-2082/1 – 390761711), by the BMBF project Open6GHub (# 16KISK010), by the Alfried Krupp von Bohlen und Halbach Foundation, by the MaxPlanck School of Photonics (MPSP), and by the Karlsruhe School of Optics & Photonics (KSOP). The authors thank Hyperlight Corp. for support in using the TFLN MZM as well as Mirko Nonnenmacher, Andreas Lipp and Steffen Pfeifer for supporting the packaging.

6. References

[1] Fontaine *et al.*, "Real-time full-field arbitrary optical waveform measurement," Nat. Photonics **4**, 248–254 (2010).
[2] Fang *et al.*, "Optical Arbitrary Waveform Measurement (OAWM) Using Silicon Photonic Slicing Filters," J. Lightw. Technol. **40**, 1705–1717 (2022).
[3] Drayss, *et al.*, "Non-sliced optical arbitrary waveform measurement (OAWM) using soliton microcombs," Optica **10**, 888–896 (2023).
[4] Fang *et al.,* "320 GHz analog-to-digital converter exploiting Kerr soliton combs and photonic-electronic spectral stitching," ECOC 2021, paper Th3C1-PD2.2.
[5] Zazzi *et al.,* "Optically Enabled ADCs and Application to Optical Communications," IEEE J. Solid-State Circuits **1**, 209–221 (2021).
[6] P. Ghelfi *et al.*, „A fully photonics-based coherent radar system," Nature **507**, 341-345 (2014).
[7] Drayss *et al.*, "Non-sliced optical arbitrary waveform measurement (OAWM) using a silicon photonic receiver chip," arXiv (to be published)
[8] Liu, *et al.*,"Ultralow-power chip-based soliton microcombs for photonic integration," Optica **5**, 1347–1353 (2018).
[9] Blaicher *et al.*, "Hybrid multi-chip assembly of optical communication engines by in situ 3D nano-lithography," Light Sci Appl **9**, 71 (2020)
[10] Nesic et al., "Ultra-broadband polarisation beam splitters and rotators based on 3D-printed waveguides," Light: Adv. Manuf. **4**, 22 (2023).
[11] Drayss, *et al.* (2023), Supplementary document for non-sliced optical arbitrary waveform measurement (OAWM) using soliton microcombs.